ARTICLE

Growth, Microstructure, and Infrared-Ultraviolet Optical Conductivity of $La_{0.5}Sr_{0.5}CoO_3$ Nanocrystalline Films on Silicon Substrates by Pulsed Laser Deposition

W. W. Li,[†] Z. G. Hu,*[,†] Y. W. Li,[†] M. Zhu,*[,‡] Z. Q. Zhu,[†] and J. H. Chu[†]

Key Laboratory of Polar Materials and Devices, Ministry of Education, East China Normal University, Shanghai 200241, People's Republic of China, and Department of Physics, Shanghai Jiao Tong University, Shanghai 200240, People's Republic of China

ABSTRACT $La_{0.5}Sr_{0.5}CoO_3$ (LSCO) nanocrystalline (nc) films have been directly grown on silicon wafers under different substrate temperatures by pulsed laser deposition. The X-ray diffraction analysis indicate that the films are polycrystalline with the pure perovskite phase at higher substrate temperatures. The columnar growth formation with the nanocrystalline structure in the films has been confirmed by microscopy experiments. Infrared−ultraviolet optical properties of the LSCO films have been investigated with the aid of spectroscopic ellipsometry (SE). Dielectric function in the photon energy range of 1.1−3.1 eV (400−1100 nm) has been extracted by reproducing the experimental data with a Lorentz oscillator model. It is found that the real part is decreased from 4.7 to −0.7 at the near-infrared region with increasing substrate temperature. The optical conductivity shows a different variation trend for the lower and higher growth temperatures, respectively. Note that the films deposited above 650 °C exhibit the well-defined metallic phase behavior. The discrepancies could be mainly ascribed to different crystalline structure and surface morphology. The present results may be crucial for future applications of ferromagnetic-based optoelectronic and spin-electronic devices.

KEYWORDS: $La_{0.5}Sr_{0.5}CoO_3$ • optical properties • dielectric functions • spectroscopic ellipsometry

1. INTRODUCTION

Ferroelectric (FE) films and devices have received much attention because of their potential technological applications in dynamic random access memories (DRAMs), electro-optic switches, pyroelectric detectors, and optical mixers (1−3). As we know, top and bottom electrodes play an important role in optoelectronic and spin-electronic devices in order to deal with electrical and/or optical signal (4−6). The physical properties of the electrode materials directly affect the device performance and efficiency. As the electrodes for perovskite FE-based optoelectronic devices, $YBa_2Cu_3O_7$ (YBCO), $SrRuO_3$, and $LaNiO_3$ materials have been widely studied as alternatives for platinum (Pt) and Pt-based metals (7−9). It is because metal oxides can be used to improve the physical properties of FE materials, as compared with noble metal electrodes (10, 11). Among the transition-metal (TM) oxides, $La_{1-x}Sr_xCoO_3$ exhibits diverse magnetic and transport properties with spin-state transitions. Especially for $x > 0.2$, it becomes metallic and associated with long-range magnetic order below a critical temperature (T_c) (12, 13). It can be expected that $La_{1-x}Sr_xCoO_3$ has much better metallic and magnetic properties because of different Sr compositions, which can be tunable if required.

$La_{1-x}Sr_xCoO_3$ has a relative large absorption coefficient and shows a more promising application in infrared detectors, playing the roles of both electrode and thermal absorption layer. Considering the potential applications of perovskite materials to optoelectronic and spin-electronic devices, the control of film orientation associated with the FE polarization states is prerequisite. Moreover, the crystalline orientation can result in the variations of optical response because of intrinsic anisotropic properties from the perovskite structure. Recently, some attention has been drawn to the highly conductive perovskite metallic oxide $La_{0.5}Sr_{0.5}CoO_3$ (LSCO) films with large magnetoresistance (14−17). This is because LSCO is a distorted perovskite with a cubic lattice parameter of 3.83 Å, which matches well with FE films such as $PbZr_{1-x}Ti_xO_3$ (PZT) and $Ba_{1-x}Sr_xTiO_3$ (BST). Keep in mind that FE films can be applied in optoelectronic devices and systems, optical response behavior of LSCO electrode is as crucial as those of FE materials. When LSCO material with controlled orientation is applied to electronic devices, it should satisfy the requirements not only as an electrode but also as an intermediate layer between the FE film and the substrate.

Owing to an increasing interest of nanostructured FE materials (18, 19), the physical properties of matched nanostructured electrodes should be further investigated in order to clarify their functions. In spite of the promising properties up to now (4, 20), there are no reports on dielectric function

* Corresponding authors. E-mail: zghu@ee.ecnu.edu.cn (Z.G.H.); zhumin@sjtu.edu.cn. (M.Z.).

Received for review December 8, 2009 and accepted February 11, 2010

[†] East China Normal University.

[‡] Shanghai Jiao Tong University.

DOI: 10.1021/am900868a

Published on Web 03/05/2010

and optical conductivity of nanostructured LSCO material, which can predictively reflect the electrical transport properties and electronic band structure. It is well-known that bulk dielectric function and/or optical conductivity can be directly related to the electronic band structure of these oxide materials. By optical conductivity analysis, one can further clarify the electronic bands, phase transitions, and free carrier plasma behavior in the TM oxides (21). Because the dielectric function plays a critical role in design, optimization, and evaluation of optoelectronic devices, it is desirable to carry out a delicate study regarding these essential properties of the LSCO material. In particular, the optical properties could be remarkably different from the bulk crystal for the LSCO material with a low-dimensional structure formation. Spectroscopic ellipsometry (SE), which is sensitive to ultrathin films and surfaces, is a nondestructive and powerful technique to investigate the optical characteristics of materials (22, 23). It is very useful to measure the thickness and dielectric function of a multilayer system simultaneously without the Kramers–Krönig transformation (KKT) (24–26). Note that SE can directly provide optical band gap, dielectric constants, and optical conductivity (27–29). This makes it possible to investigate the optical function of the present nanocrystalline LSCO films in a wider photon energy range.

In this article, the dielectric function of nanostructured LSCO films grown under different substrate temperatures (T_s) has been studied in the photon energy range of 1.1–3.1 eV. The growth parameter effects on the optical conductivity have been discussed in detail. The present objective is to obtain the relationship between optical function and crystalline structure of the low-dimensional LSCO films.

2. EXPERIMENTAL SECTION

Growth of the LSCO Films. Nanocrystalline (nc) LSCO films were deposited on single-side polished silicon (100) wafers by pulsed laser deposition. The substrates were cleaned in pure ethanol with an ultrasonic bath to remove physisorbed organic molecules from the Si surfaces. Then the substrates were rinsed several times with deionized water. Finally the wafers were dried in a pure nitrogen stream before the deposition of the LSCO films. A KrF excimer laser was used for the deposition with the pulse frequency of 5 Hz. The ceramic LSCO target with a La:Sr stoichiometric ratio of 0.5:0.5 was sintered by solid-state reaction. The oxygen pressure was controlled at 25 Pa during the entire deposition process. The T_s was kept at 500–700 °C with an interval of 50 °C, which indicates that five film samples have been fabricated in the present work. In order to obtain the similar thickness for a comparison, the LSCO layers have been deposited during the several periods because the growth rate is different from lower and higher T_s.

XRD, AFM, SEM, and SE Measurements. The crystalline structure of the LSCO films was analyzed by X-ray diffraction (XRD) using Cu $K\alpha$ radiation (D/MAX- 2550 V, Rigaku Co.). In the XRD experiments, a vertical goniometer (model RINT2000) was used and continuous scanning mode ($2\theta/\theta$) was selected with an interval of 0.02° and scanning rate of 10°/min. The surface morphology was investigated by atomic force microscopy (AFM) (Digital Instruments Dimension 3100, Veeco). The roughness of the LSCO films was characterized with the contacting mode in areas of 5 × 5 μm^2. The surface and cross-sectional microstructures of the films were studied by scanning electron microscopy (SEM). Ellipsometric spectra have been measured in the photon energy region of 1.1–3.1 eV (400–1100 nm) with a spectral resolution of 5 nm by near-infrared-ultraviolet SE (SC630UVN by Shanghai Sanco Instrument, Co., Ltd.). The system operations, including data acquisition, incident angle, wavelength setting, and scanning, were automatically controlled by the computer. The measurements were carried out at the incident angles of 65, 70, and 75°. The samples were at room temperature (RT) for all measurements and no mathematical smoothing has been performed for the experimental data.

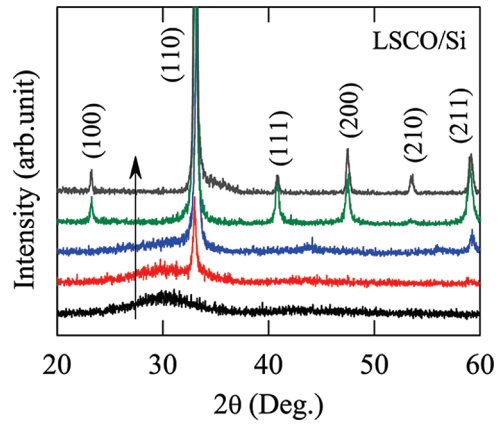

FIGURE 1. XRD patterns of $La_{0.5}Sr_{0.5}CoO_3$ films grown on Si substrates. The arrow indicates that the films become better crystalline with increasing substrate temperature. Note that the (110) diffraction peak for 650 and 700 °C is cut because of the much stronger intensity.

3. RESULTS AND DISCUSSION

Structural Characterization. The XRD patterns of LSCO films grown on Si (100) wafers at different T_s values are shown in Figure 1. As we can see, the film grown at 500 °C is amorphous with the broad diffraction peak near 30°. A weaker (110) diffraction peak appears at 33° for the sample grown under 550 °C. It indicates that the LSCO film shows evidence of crystal information at T_s of 550 °C. With increasing T_s, the intensity of (110) peak becomes stronger and (211) peak appears; however, the amorphous component can be still observed. For two film samples grown at 650 and 700 °C, they are fully crystallized. Besides the strongest (110) peak, some weaker peaks (100), (111), (200), (210), and (211) are present, which indicate that the LSCO films are polycrystalline. In particular, the (110) diffraction peak becomes much stronger, as compared to the intensity of (100) and (111) peak for the film at 700 °C. The striking increment for the film deposited at 700 °C could be due to the better crystallization.

For nanostructured materials, the grain size (r) plays an critical role in the physical properties. According to the following Scherrer equation: $r = K\lambda/\delta\cos\theta$ (31, 32). Here, $K \approx 1$ is the shape factor, $\lambda = 1.540$ Å is the average wavelength of Cu $K\alpha$ radiation, δ is the full width at half-maximum (fwhm), and θ is the diffraction angle, the grain size of the LSCO films from the (110) peak was evaluated to about 26, 28, 27, and 49 nm with increasing T_s except for the sample grown at 500 °C, which has no obvious diffraction peak. For a comparison, the values are listed in Table 1. The striking increment for the film deposited at 700 °C

Table 1. Drude–Lorentz Parameter Values of $La_{0.5}$ $Sr_{0.5}$ CoO_3 Films Determined from the Simulation of Ellipsometric Spectra in Figures [4] and [5,a]

samples	T_s (°C)	grain size r (nm)	ε_∞	A_1 (eV^2)	B_1 (eV)	E_1 (eV)	A_2 (eV^2)	B_2 (eV)	E_2 (eV)
A	500		0.71 ± 0.22	445 ± 154	22.4 ± 5.4	10.6 ± 1.5	0.12 ± 0.01	0.32 ± 0.01	1.23 ± 0.01
B	550	26	1.30 ± 0.13	138 ± 25	10.3 ± 1.2	6.29 ± 0.45	0.36 ± 0.05	0.89 ± 0.08	1.24 ± 0.01
C	600	28	0.42 ± 0.56	216 ± 167	10.3 ± 5.9	7.40 ± 1.95	4.45 ± 4.81	3.74 ± 2.29	1.82 ± 0.64
D	650	27	2.63 ± 0.03	27 ± 1	3.8 ± 0.1	2.33 ± 0.01	7.78 ± 0.18	0.64 ± 0.04	0[b]
E	700	49	2.32 ± 0.03	23 ± 1	3.5 ± 0.1	2.04 ± 0.01	8.12 ± 0.15	0.34 ± 0.03	0[b]

[a] The 90% reliability of the fitting parameters is given with (±). [b] These values were fixed in the fitting calculation.

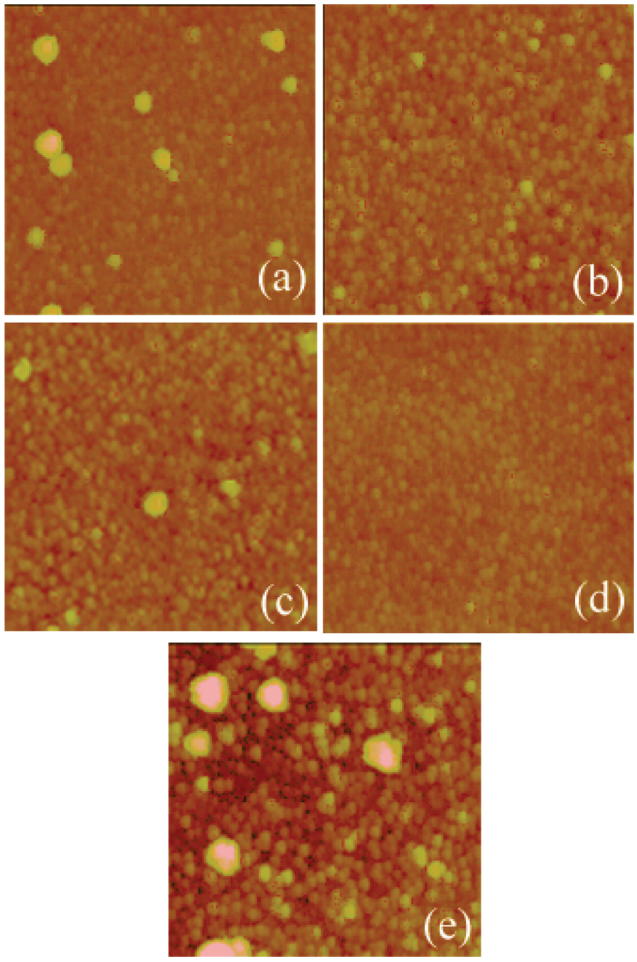

FIGURE 2. AFM two-dimensional images of $La_{0.5}Sr_{0.5}CoO_3$ films grown at (a) 500, (b) 550, (c) 600, (d) 650, and (e) 700 °C, respectively. Note that the scale height is 200 nm and the measured area is 5 × 5 μm^2. The average rms roughness is estimated to about 10 nm.

could be due to the better crystallization, which was confirmed by the AFM results as shown in Figure 2. The surface morphology becomes more prominent, indicating that the surface roughness is increased with increasing T_s. Note that the surface roughness is maximum for the LSCO film deposited at 700 °C. The average root-mean-square (rms) roughness is estimated to about 10 nm. The increasing surface roughness can be ascribed to a higher T_s, which makes the LSCO film more dense and some voids appear on the surface.

The surface and cross-sectional SEM images from the LSCO films grown at 650 and 700 °C have been presented in Figure 3. The results suggest that the LSCO films are of

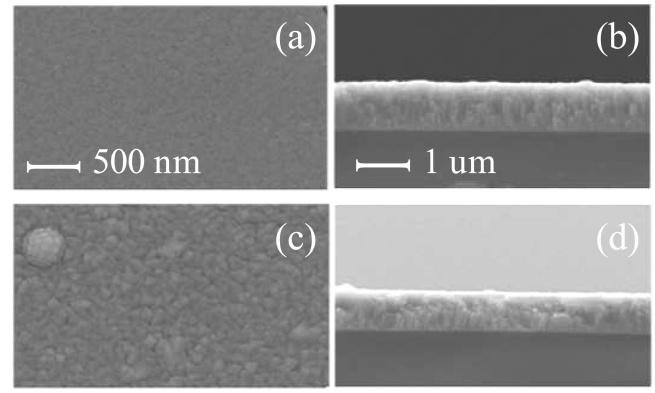

FIGURE 3. (a, c) Surface and (b, d) cross-sectional SEM images of $La_{0.5}Sr_{0.5}CoO_3$ films grown at 650 and 700 °C, respectively. Note that the scale is given in the pictures.

the columnar growth formation with the diameter of about several tens of nanometers (30). From the cross-sectional images, the thickness of the films is evaluated to about 1 μm, which agrees well with the nominal growth values. It should be emphasized that the film thickness is nearly the same for the LSCO films deposited at five T_s due to different deposition periods, as previously discussed. From the SEM surface and AFM images, it can be concluded that the LSCO films have the nanocrystalline growth pattern. Nevertheless, an obvious difference of grain size among the films grown at different T_s can be observed from the microscopic images. It indicates that the growth parameter T_s can directly affect the crystalline structure and surface morphology of the LSCO films. The remarkable discrepancy of the surface morphology between the films grown at two higher T_s can result in the variation of optical and electrical properties.

Theoretical Consideration. SE deals with the measurement of the relative changes in the amplitude and phase of the s- and p-components of linearly polarized light upon oblique reflection from the sample surface (29). The experimental quantities measured by ellipsometry are the angles Ψ and Δ, which are related to the optical and structure properties of the samples, are defined by

$$\rho \equiv \frac{\tilde{r}_p}{\tilde{r}_s} = \tan \Psi \exp(i\Delta) \quad (1)$$

Here, $\tilde{r}_p$ and $\tilde{r}_s$ are the complex reflection coefficients of the light polarized parallel and perpendicular to the plane of incidence, respectively. Note that ρ is the function of thickness, photon frequency, and optical constants from the

system studied. Because of the relatively thick LSCO films (about 1 μm), the semi-infinite medium approach can be used to directly derive the dielectric function:

$$\tilde{\varepsilon} = \sin^2\varphi[1 + (1 - \rho)^2/(1 + \rho)^2\tan^2\varphi] \qquad (2)$$

Here, φ is the incident angle. The above equation indicates that the incident light cannot reach the interface between the film and substrate, whose effects on the optical reflection could be neglected. However, a dispersion model with the physical meaning is still necessary for interpreting the experimental ellipsometric data (24, 29). Because of the conductivity of LSCO films, the dielectric function can be expressed using a Lorentz oscillator dispersion relation (7, 8, 21, 28)

$$\tilde{\varepsilon}(E) = \varepsilon_r + i\varepsilon_i = \varepsilon_\infty + \sum_{k=1}^{2} \frac{A_k}{E_k^2 - E^2 - iEB_k} \qquad (3)$$

Where ε_∞ is the high-frequency dielectric constant, A_k, E_k, B_k, and E is the amplitude, center energy, broadening of the kth oscillator, and the incident photon energy, respectively (7, 21). Note that when E_k is equal to zero, the model is transformed to the known Drude function (Here, A_k is the square of the plasma frequency, B_k is electron collision or damping frequency). The best-fit parameter values in eq 3 can be nonlinear calculation method for many parameter fitting (25, 33). It is widely accepted that the Lorentz oscillator dielectric function can be suitable in expressing the dispersion relation in the transparent region for most of semiconductors and insulators. However, the present LSCO films are conductive oxides and show the metal-like behavior. Generally, the optical functions of nobel metals and conductive oxides can be described by the Lorentz oscillator model, which corresponds to different interband and intraband electronic transitions (34−37). As previously discussed, the dielectric functions of the LSCO films, which are not dependent on the Lorentz oscillator model selection, can be directly derived from the experimental SE data with a two-phase structure model, i.e., eq 2.

Generally, the surface rough layer could be several nanometers (about 10 nm for the LSCO film grown at 700 °C), which is much less than the film thickness (about 1 μm). From the AFM and SEM figures, the surfaces of the films are compact and the interfaces are distinct. It is found that the density of the LSCO film surface is different with the T_s. In addition, too many fitting parameters will result in strong correlation coefficient and make the convergence difficult in the SE fitting calculation. Therefore, the surface rough layer is neglected because of a smaller thickness value, whose contribution should be slight in the evaluation of the optical properties. In particular, for the LSCO conductive films, the optical response is mainly from free carrier behavior, which can strongly screen other effects, such as the surface roughness. Thus, an effective medium theory model is not applied in the fitting calculation. It should be

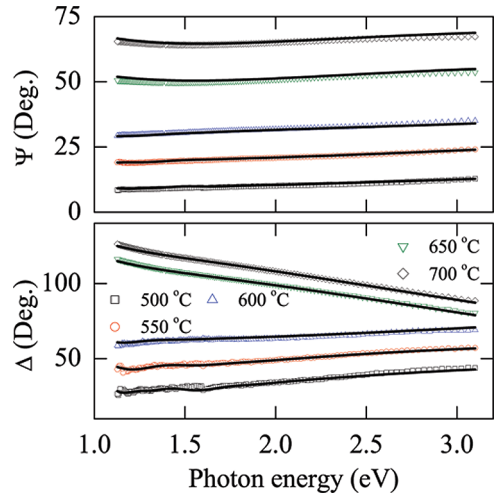

FIGURE 4. Experimental (dotted lines) and best-fit (solid lines) values for the Ψ and Δ spectra of $La_{0.5}Sr_{0.5}CoO_3$ films from near-infrared to ultraviolet photon energy region at the incident angle of 70°. Both Ψ and Δ data are vertically shifted by adding 10°.

emphasized that the optical anisotropy can be neglected in the SE experiments because LSCO is a distorted perovskite with a cubic lattice structure. On the other hand, the difference between the lattice constants of perovskite crystalline along the c (tetragonal) and a (cubic) axis is only 1 % at RT (38).

Ellipsometric Spectra. As an example, the experimental ellipsometric spectra of the LSCO films at the incident angles of 70° are shown in Figure 4 with the dotted lines. Generally, the SE spectra recorded at three incident angles show the similar dependence on the photon energy except for the amplitude, which is slightly increased with the incident angle. Note that the dielectric function $\tilde{\varepsilon}$, which can be derived with eq 2 from the SE data at three incident angles, is the same within experimental error. It indicates that the effects from the substrate can be neglected because of the relatively thick film. The Ψ value is increased with the photon energy for the three samples at lower T_s. However, the angle value begins to decrease and increases with the photon energy for two films at the higher T_s. Note that there is a dip near the photon energy of 1.6 eV. On the other hand, the phase Δ presents a completely different variation trend. The LSCO films deposited at lower T_s slightly increases with the photon energy. In particular, the spectra from two films at the higher T_s decrease with increasing photon energy. It indicates that the films grown at 650 and 700 °C have a distinct optical response behavior. It can be concluded that the observed changes in the optical SE data Ψ and Δ are due to different film density, which shows a decreasing trend as the T_s increases. The reproduced SE results with the Lorentz model parameters are also shown in Figure 4 by the solid lines and the values are given in Table 1. A good agreement is obtained between the experimental and calculated spectra in the entirely measured photon energy range.

As we know, the perovskite oxide materials have a relatively complicated electronic structure, which covers the photon energy from near-infrared to ultraviolet wavelength.

The number of optical transition used in the simulation can be related to the physical properties of the LSCO films. In the present work, the photon energy range is located between 1.1 and 3.1 eV because of the SE experimental limitation. Therefore, two oscillators can be applied to express the optical response of the LSCO films, which correspond to different interband/intraband electronic transitions (37). Also, the fitted parameters give a detailed transition process from insulator to conductor with increasing T_s for the LSCO films. The results are consistent with the XRD data. It should be emphasized that the E_1 values can be more suitable for the two higher T_s than those at lower T_s. This is because the E_1 values for the films at lower T_s are far away from the measured photon energy. As compared with the theoretical model of the band structure for the metallic oxides (39), the E_1 energy band (2.33 ± 0.01 and 2.04 ± 0.01 eV) for sample D and E can be assigned to the electronic transition of t_{2g} and the Jahn−Teller (JT) effect (37). Note that the parameter E_2 for the films at 650 and 700 °C nearly approaches zero when they are defined as the fitting variables. It indicates that the two films are well-conductive and the contributions from the Drude response become more prominent. Therefore, the E_2 values for the above two films are fixed to zero in order to decrease the correlation coefficient in the fitting calculations. Nevertheless, the E_2 is fitted to 1.23 ± 0.01, 1.24 ± 0.01, and 1.82 ± 0.64 eV for the films at 500, 550, and 600 °C, respectively. These values are closer to the experimental near-infrared region. Correspondingly, it can be concluded that the growth temperature plays an important role in the optical and electrical properties for the LSCO films.

Dielectric Function. Although the optical features at low energy are generally related to electric and magnetic properties, it was found that the electronic band structure at high energy is as important as the low-energy characteristics (39). The evolution of $\tilde{\varepsilon}$ with the photon energy shows a different optical response behavior for the lower and higher T_s, respectively. Below the temperature of 600 °C, the real part ε_r decreases with the photon energy and the values for the three samples are evaluated to be about 4.7 at 1.1 eV, as shown in Figure 5a. However, the ε_r, which is strikingly smaller for the temperatures of 650 and 700 °C, is about 1.1 and −0.7 at the near-infrared region, respectively. To give a further insight on the electronic structure and optical conductivity σ of the LSCO films, the real part can be calculated by $\sigma_r = \varepsilon_0\omega\varepsilon_i$, here ε_0 and ω is the vacuum dielectric constant and the light frequency, respectively. Figure 5b gives the real part of optical conductivity σ_r from the LSCO films at different T_s. Again, the optical conductivity presents the different behavior for two growth temperature regions. Below the T_s of 650 °C, the σ_r linearly increases with the photon energy and approaches a maximum value of about $1 \times 10^3\ \Omega^{-1}\ cm^{-1}$ near the ultraviolet region.

There is a broadening peak near 1.6 eV in the films at higher T_s, which can be ascribed to the electronic transition from a d^6 ground state to the d^5 final state of the cobalt ion and the strong crystal-field limit (21). This is essentially a

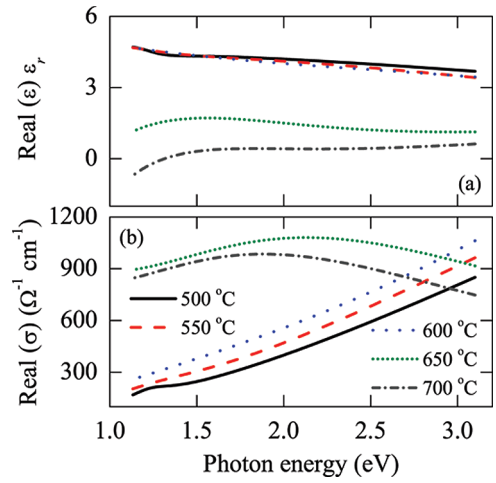

FIGURE 5. Real parts of (a) dielectric function and (b) optical conductivity for $La_{0.5}Sr_{0.5}CoO_3$ films at different substrate temperatures in the photon energy range of 1.1−3.1 eV. Note that there is a remarkable transition for the films deposited at 650 and 700 °C. There are the undistinguished ε_r results for the films grown at three lower T_s values.

charge-transfer hopping between nearest-neighbor cobalt ions (40). The observation agrees well with the result for the LSCO material, where a slight dip appears from optical reflectance measurement (20). Moreover, the charge transfer energy between the O 2p and the Co 3d states are evaluated to be in the order of 1 eV. Therefore, the peak near 1.6 eV could be also related to the p−d electronic transition (41). The optical conductivity then rapidly decreases with further increasing the photon energy. Nevertheless, the value is located to be about $1 \times 10^3\ \Omega^{-1}\ cm^{-1}$ in the entirely experimental region. The observed value magnitude suggests that the JT related excitation bands appear in the present LSCO films, which occurs in some crystalline TM oxide films (39, 42). It is well-known that there is an evidence that the strong JT effect from the Co ions is important and results in the lattice distortion in the undoped material (39). It is further confirmed that the films are crystalline from the XRD patterns. Note that the conductive behavior for the two LSCO films grown at higher T_s is similar to those of high-temperature superconductivity (20, 43). Optical experiments at far-infrared wavelengths under low temperatures are necessary to further clarify the physical behavior.

Optical Conductivity. Note that the variation physical parameter is the growth temperature in the present work. It indicates that the deposition conditions play an important role in the optical and electrical properties for the LSCO films. Nevertheless, the nc-LSCO films present a disparate structure for different growth conditions. It was reported that the structural distortions can affect the electronic band structures of the perovskite-type materials (44). On the basis of the XRD peaks (110), (200), and (211), the films deposited at lower T_s are partly crystalline and contain some amorphous phase. Their optical conductivity is much worse and does not show the well-defined metallic phase. Furthermore, the crystalline orientation is slightly different, compared to the two films at higher T_s. Because of the different fwhm from the (110) peak, the average grain size could be diverse

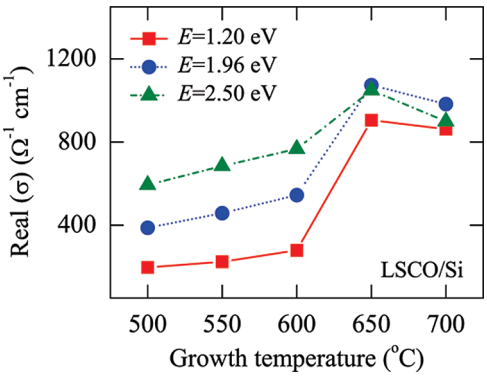

FIGURE 6. Variations in the real part of optical conductivity in $La_{0.5}Sr_{0.5}CoO_3$ films with the substrate temperature at the photon energy of 1.20, 1.96, and 2.50 eV, respectively. The straight lines are only used to guide the eyes.

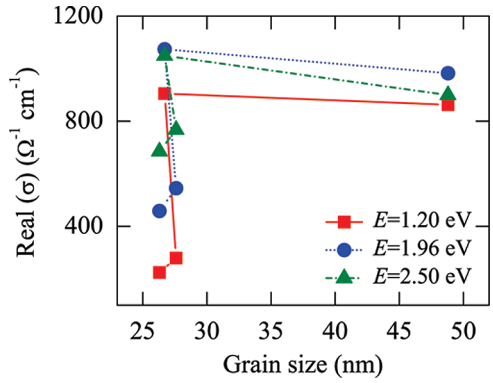

FIGURE 7. Grain size dependence of the optical conductivity for $La_{0.5}Sr_{0.5}CoO_3$ films at photon energies of 1.20, 1.96, and 2.50 eV, respectively. Note that there is a different conductivity from the grain size variation.

with increasing T_s. The discrepancy can contribute to the variation of the optical conductivity.

At higher T_s, the silicon diffusion into the films becomes dominant, and a cation (Si^{4+}) doping may be responsible for the phenomena observed, which is supported by an unexpected broadening near the (110) diffraction peak at $2\theta \approx 36°$ (see Figure 1). Therefore, the slight diffusion also can result in the optical conductivity variations. To be compatible with mature silicon-based microelectronic techniques, the T_s parameter needs to be taken into account to produce the FE optoelectronic devices. On the other hand, the electronic structures appearing near the bottom of the valence band in both e_g and t_{2g} bands, which are covalent contributions originating from the Co−O bonds in the distorted cubic structure, can be perturbed owing to the O 2p orbitals (42). The slightly different cubic crystalline due to the T_s can contribute to the electronic structures of the LSCO films, which results in the optical conductivity changes. Therefore, it can be believed that the optical conductivity discrepancy is mainly ascribed to the different crystalline quality and surface morphology. Figure 6 shows the T_s dependence of the optical conductivity at different photon energies. Although there is an obvious difference, the optical conductivity trends to a uniform value at higher T_s. It clearly indicates that the crystalline quality has a prominent contribution to the physical properties. The optical conductivity shows a remarkable transition with the growth temperature, i.e., the crystalline formation. In addition, given the skin depth for the penetration of light in the LSCO films, the optical conductivity values at different photon energy can be used to confirm the validity of the semi-infinite medium approach. It indicates that the thick nc-LSCO films are uniform and dense, as seen in Figures 2 and 3. On the other hand, the optical conductivity increases with increasing growth temperature as the decomposition pressure of the constituents increases. It will induce a higher point defect density and higher free carrier concentrations, which results in the optical conductivity variations.

The grain size dependence of the optical conductivity has been given in Figure 7. It can be concluded that the average grain size can affect the conductivity of the LSCO films. Although the grain size variation is due to different T_s values, the physical properties are directly related to the crystalline structure from the present results. The optical conductivity shows a remarkable transition with the grain size. For a small grain size, the T_s can induce the crystallization, which plays an important role in the conductivity. With increasing grain size, the T_s influence is suppressed and some other factors, such as grain size and grain boundary, contribute to the conductivity (45). A more rigorous estimation method for the grain size, which contains the instrumental broadening and/or microstrain contribution to the fwhm, is necessary to further clarify the influences. The ability of the columnar grain boundaries to depolarize the detected polarizing light is different if the surface morphology is not the same. The interaction between the grain boundaries and/or morphologies and the incident light changes with different columnar structure states. Finally, the Drude item of the function model, which is directly related to the direct current (dc) electrical transport, is proportional to the parameter ratio (B_2/A_2) (7). By comparing the fitting values of Sample D and E in Table 1, one can conclude that the LSCO film grown at higher T_s has a smaller dc resistivity. This agrees well with the electrical resistivity recorded by the standard dc four-probe method (30). This could be an important factor for characterizing the top and bottom electrodes in the FE-based optoelectronic devices.

4. CONCLUSIONS

The nc-LSCO films with the thickness of about 1 μm were deposited on silicon substrates at different growth temperatures by pulsed laser deposition. The substrate temperature dependence of optical properties has been simultaneously determined from the near-infrared to ultraviolet region by the SE technique at three incident angles of 65, 70, and 75°. The dielectric function with the photon energy shows a completely different optical response behavior for the lower and higher growth temperatures. It is found that the optical conductivity trends to a uniform value of about $1 \times 10^3\ \Omega^{-1}\ cm^{-1}$ at higher substrate temperature. The optical conductivity discrepancy can be mainly ascribed to the different crystalline quality. The present investigations suggest that the substrate temperature could be one of the crucial factors,

which directly affect the electrical and optical properties of nanostructured conductive metallic oxides.

Acknowledgment. The authors acknowledge Professor Xiaodong Tang and Mr. Junyu Zhu for the AFM experiments and technical support. This work was financially sponsored by Natural Science Foundation of China (Grant 60906046), Major State Basic Research Development Program of China (Grant 2007CB924901), Program of New Century Excellent Talents, MOE (Grant NCET-08-0192), Shanghai Municipal Commission of Science and Technology Project (Grants 08JC1409000, 08520706100, and 09ZZ42).

REFERENCES AND NOTES

(1) Ahn, C. H.; Rabe, K. M.; Triscone, J.-M. *Science* **2004**, *303*, 488.
(2) Scott, J. F. *Science* **2007**, *315*, 954.
(3) Shin, H.; Chang, H. J.; Boyd, R. W.; Choi, M. R.; Jo, W. *Opt. Lett.* **2007**, *32*, 2453.
(4) Ramesh, R.; Lee, J.; Sands, T.; Keramidas, V. G.; Auciello, O. *Appl. Phys. Lett.* **1994**, *64*, 2511.
(5) Yang, B.; Aggarwal, S.; Dhote, A. M.; Song, T. K.; Ramesh, R.; Lee, J. S. *Appl. Phys. Lett.* **1997**, *71*, 356.
(6) Imamura, M.; Matsubayashi, N.; Shimada, H. *J. Phys. Chem. B* **2000**, *104*, 7348.
(7) Hu, Z. G.; Huang, Z. M.; Wu, Y. N.; Zhao, Q.; Wang, G. S.; Chu, J. H. *J. Appl. Phys.* **2004**, *95*, 4036.
(8) Berini, B.; Keller, N.; Dumont, Y.; Popova, E.; Noun, W.; Guyot, M.; Vigneron, J.; Etcheberry, A.; Franco, N.; Rui da Silva, M. C. *Phys. Rev. B* **2007**, *76*, 205417.
(9) McKinlay, A.; Connor, P.; Irvine John, T. S.; Zhou, W. Z. *J. Phys. Chem. C* **2007**, *111*, 19120.
(10) Angadi, M.; Auciello, O.; Krauss, A. R.; Gundel, H. W. *Appl. Phys. Lett.* **2000**, *77*, 2659.
(11) Le Rhun, G.; Poullain, G.; Bouregba, R. *J. Appl. Phys.* **2004**, *96*, 3876.
(12) Xiong, Y. M.; Chen, X. H.; Luo, X. G.; Wang, C. H.; Song, H. B.; Chen, C. L.; Chang, H. Y. *J. Phys.: Condens. Matter* **2004**, *16*, 553.
(13) Fuchs, D.; Schwarz, T.; Morán, O.; Schweiss, P.; Schneider, R. *Phys. Rev. B* **2005**, *71*, 092406.
(14) Briceno, G.; Chang, H.; Sun, X.; Schultz, P. G.; Xiang, X.-D. *Science* **1995**, *270*, 273.
(15) Hill, N. A. *J. Phys. Chem. B* **2000**, *104*, 6694.
(16) Rossel, C.; Rosová, A.; Hueková, K.; Machajdík, D.; Fröhlich, K. *J. Appl. Phys.* **2006**, *100*, 044501.
(17) Xie, C. K.; Budnick, J. I.; Wells, B. O.; Woicik, J. C. *Appl. Phys. Lett.* **2007**, *91*, 172509.
(18) Naumov, I. I.; Bellaiche, L.; Fu, H. *Nature* **2004**, *432*, 737.
(19) Kim, J.; Yang, S. A.; Choi, Y. C.; Han, J. K.; Jeong, K. O.; Yun, Y. J.; Kim, D. J.; Yang, S. M.; Yoon, D.; Cheong, H.; Chang, K.-S.; Noh, T. W.; Bu, S. D. *Nano Lett.* **2008**, *8*, 1813.
(20) Bozovic, I.; Kim, J. H.; Harris, J. S., Jr.; Eom, C. B.; Phillips, J. M.; Cheung, J. T. *Phys. Rev. Lett.* **1994**, *73*, 1436.
(21) Gössling, A.; Haverkort, M. W.; Benomar, M.; Wu, H.; Senff, D.; Möller, T.; Braden, M.; Mydosh, J. A.; Grüninger, M. *Phys. Rev. B* **2008**, *77*, 035109.
(22) Hinrichs, K.; Tsankov, D.; Korte, E. H.; Röseler, A.; Sahre, K.; Eichhorn, K. J. *Appl. Spectrosc.* **2002**, *56*, 737.
(23) Tompkins, H. G.; Tiwald, T.; Bungay, C.; Hooper, A. E. *J. Phys. Chem. B* **2004**, *108*, 3777.
(24) Hinrichs, K.; Gensch, M.; Esser, N. *Ap pl. Spectrosc.* **2005**, *59*, 272A.
(25) Hu, Z. G.; Prunici, P.; Patzner, P.; Hess, P. *J. Phys. Chem. B* **2006**, *110*, 14824.
(26) Hu, Z. G.; Li, Y. W.; Zhu, M.; Zhu, Z. Q.; Chu, J. H. *J. Phys. Chem. C* **2008**, *112*, 9737.
(27) Kasic, A.; Schubert, M.; Einfeldt, S.; Hommel, D.; Tiwald, T. E. *Phys. Rev. B* **2000**, *62*, 7365.
(28) Qazilbash, M. M.; Schafgans, A. A.; Burch, K. S.; Yun, S. J.; Chae, B. G.; Kim, B. J.; Kim, H. T.; Basov, D. N. *Phys. Rev. B* **2008**, *77*, 115121.
(29) Azzam R. M. A.; Bashara N. M. *Ellipsometry and Polarized Light*; North-Holland: Amsterdam, 1977.
(30) Li, Y. W.; Hu, Z. G.; Yue, F. Y.; Zhou, W. Z.; Yang, P. X.; Chu, J. H. *Appl. Phys. A: Mater. Sci. Process.* **2009**, *95*, 721.
(31) Cullety B. D. *Elements of X-ray Diffraction*; Addison-Wesley: Reading, MA, 1978.
(32) Wilson, A. J. C. *Proc. Phys. Soc. (London)* **1962**, *80*, 286.
(33) Press, W. H.; Teukolsky, S. A.; Vetterling, W. T.; Flannery, B. P. *Numerical Recipes in C: The Art of Scientific Computing*; Cambridge University Press: Cambridge, MA, 1992.
(34) Kovaleva, N. N.; Boris, A. V.; Bernhard, C.; Kulakov, A.; Pimenov, A.; Balbashov, A. M.; Khaliullin, G.; Keimer, B. *Phys. Rev. Lett.* **2004**, *93*, 147204.
(35) Seo, S. S. A.; Choi, W. S.; Lee, H. N.; Yu, L.; Kim, K. W.; Bernhard, C.; Noh, T. W. *Phys. Rev. Lett.* **2007**, *99*, 266801.
(36) Noun, W.; Berini, B.; Dumonta, Y.; Dahoo, P. R.; Keller, N. *J. Appl. Phys.* **2007**, *102*, 063709.
(37) Hu, Z. G.; Li, W. W.; Li, Y. W.; Zhu, M.; Zhu, Z. Q.; Chu, J. H. *Appl. Phys. Lett.* **2009**, *94*, 221104.
(38) Hu, Z. G.; Li, Y. W.; Zhu, M.; Zhu, Z. Q.; Chu, J. H. *Phys. Lett. A* **2008**, *372*, 4521.
(39) Rusydi, A.; Rauer, R.; Neuber, G.; Bastjan, M.; Mahns, I.; Müller, S.; Saichu, P.; Schulz, B.; Singer, S. G.; Lichtenstein, A. I.; Qi, D.; Gao, X.; Yu, X.; Wee, A. T. S.; Stryganyuk, G.; Dörr, K.; Sawatzky, G. A.; Cooper, S. L.; Rübhausen, M. *Phys. Rev. B* **2008**, *78*, 125110.
(40) Quijada, M. A.; Simpson, J. R.; Vasiliu-Doloc, L.; Lynn, J. W.; Drew, H. D.; Mukovskii, Y. M.; Karabashev, S. G. *Phys. Rev. B* **2001**, *64*, 224426.
(41) Imada, M.; Fujimori, A.; Tokura, Y. *Rev. Mod. Phys.* **1998**, *70*, 1039.
(42) Tokura, Y.; Okimoto, Y.; Yamaguchi, S.; Taniguchi, H.; Kimura, T.; Takagi, H. *Phys. Rev. B* **1998**, *58*, R1699.
(43) Basov, D. N.; Timusk, T. *Rev. Mod. Phys.* **2005**, *77*, 721.
(44) Hu, Z. G.; Li, Y. W.; Zhu, M.; Zhu, Z. Q.; Chu, J. H. *Appl. Phys. Lett.* **2008**, *92*, 081904.
(45) Hu, Z. G.; Hess, P. *Appl. Phys. Lett.* **2006**, *89*, 081906.

AM900868A